Physiological Measurement

IPEM
Institute of Physics and Engineering in Medicine

PAPER

Correlation between alveolar ventilation and electrical properties of lung parenchyma

To cite this article: Christian J Roth *et al* 2015 *Physiol. Meas.* **36** 1211

IOP Publishing | Institute of Physics and Engineering in Medicine Physiological Measurement

Physiol. Meas. **36** (2015) 1211–1226 doi:10.1088/0967-3334/36/6/1211

Correlation between alveolar ventilation and electrical properties of lung parenchyma

Christian J Roth[1], Andreas Ehrl[1], Tobias Becher[2], Inéz Frerichs[2], Johannes C Schittny[3], Norbert Weiler[2] and Wolfgang A Wall[1]

[1] Institute for Computational Mechanics, Technische Universität München, Boltzmannstrasse 15, D-85748 Garching b. München, Germany
[2] Department of Anesthesiology and Intensive Care Medicine, Christian Albrechts University, Schwanenweg 21, D-24105 Kiel, Germany
[3] Institute of Anatomy, University of Bern, Baltzerstrasse 2, CH-3012 Bern, Switzerland

E-mail: roth@lnm.mw.tum.de, ehrl@lnm.mw.tum.de, wall@lnm.mw.tum.de, becher@anaesthesie.uni-kiel.de, frerichs@anaesthesie.uni-kiel.de, weiler@anaesthesie.uni-kiel.de and schittny@ana.unibe.ch

Received 30 November 2014, revised 24 February 2015
Accepted for publication 26 February 2015
Published 26 May 2015

Abstract

One key problem in modern medical imaging is linking measured data and actual physiological quantities. In this article we derive such a link between the electrical bioimpedance of lung parenchyma, which can be measured by electrical impedance tomography (EIT), and the magnitude of regional ventilation, a key to understanding lung mechanics and developing novel protective ventilation strategies. Two rat-derived three-dimensional alveolar microstructures obtained from synchrotron-based x-ray tomography are each exposed to a constant potential difference for different states of ventilation in a finite element simulation. While the alveolar wall volume remains constant during stretch, the enclosed air volume varies, similar to the lung volume during ventilation. The enclosed air, serving as insulator in the alveolar ensemble, determines the resulting current and accordingly local tissue bioimpedance. From this we can derive a relationship between lung tissue bioimpedance and regional alveolar ventilation. The derived relationship shows a linear dependence between air content and tissue impedance and matches clinical data determined from a ventilated patient at the bedside.

Keywords: EIT, lung impedance, tissue properties, alveolar geometry, ventilation monitoring, lung volume

(Some figures may appear in colour only in the online journal)

1. Introduction

Over the past 30 years electrical impedance tomography (EIT) has proven to be a reliable tool for monitoring physiological processes in the human body such as cardiac activity (Brown *et al* 1994, Nguyen *et al* 2012, Frerichs *et al* 2014), gastric emptying (Brown 2003), or respiration (Frerichs 2000, Bodenstein *et al* 2009, Adler *et al* 2012, Frerichs *et al* 2014). It has become especially popular in imaging regional lung ventilation, as it is the only non-invasive, radiation-free method that is suitable for long-term imaging of ventilation at the bedside.

The principle of EIT is the measurement of potential differences between electrodes on the surface of a body when small alternating currents are sent into the studied subject at high frequency. One currently used EIT system is the PulmoVista® 500 tomograph (Dräger Medical, Lübeck, Germany), which operates at a frequency of 50 kHz. Current injections take place at an adjacent pair of 16 self-adhesive surface electrodes placed circumferentially around the chest and voltage is measured at the remaining ones. When the current injection pair rotates around all electrodes, a transversal-plane image can be reconstructed from $N = 208$ voltage measurements using the back-projection algorithm by Barber (1989) or more advanced reconstruction algorithms such as the Graz consensus reconstruction algorithm for EIT (GREIT) by Adler *et al* (2009). The resulting 32×32 pixel image visualizes regional resistivity differences against a defined baseline state.

EIT performs well in lung imaging, as tissue resistivity considerably changes with ventilation. This is due to the variation of the resulting length for the current when, e.g. a higher volume of air is enclosed in the alveoli. Using this technique several groups have successfully carried out ventilation studies on neonates (Bayford *et al* 2008, Riedel *et al* 2009, Miedema *et al* 2012), adults (Victorino *et al* 2004, Erlandsson *et al* 2006, Vogt *et al* 2012, Mauri *et al* 2013, Blaser *et al* 2014), in different body positions (Reifferscheid *et al* 2011, Lupton-Smith *et al* 2014) and even in microgravity (Hahn *et al* 2013). Furthermore EIT has also proven to be suitable for interesting investigations in animal models such as those of Hinz *et al* (2003), 29, 55, 34, 54, 24] and Yoshida *et al* (2013). All these studies show remarkable results, give further insight into physiology and pathophysiology and increase understanding of respiratory function.

However, it is worth noticing that current impedance tomography observations only show relative physiological quantities. As already mentioned, the impedance change is only a relative one against a baseline image, often representing functional residual capacity (FRC) in a healthy subject or end-expiratory lung volume (EELV) at positive end-expiratory pressure (PEEP) in a ventilated patient. Besides, the impedance changes observed so far only qualitatively compare different regions of the lung, e.g. dependent and non-dependent. Still missing is a quantitative link between the measured tissue impedance and the amplitude of local ventilation, which is important for setting 'correct' ventilation parameters. First attempts towards linking these two quantities have been made by Nopp *et al* (1993) with an experimental approach on excised lungs of slaughtered calves and later (Nopp *et al* 1997) with an idealized alveolar geometry model based on a thin-walled cube. Since then several groups have stated correlations between impedance and air content in lung tissue (Schwan and Kay 1956, Rush *et al* 1963, Gabriel *et al* 1996a, 1996b, Zhang and Patterson 2010, Nebuya *et al* 2011, Wang *et al* 2014), though with high variability ranging from 3.4 Ωm to 28.6 Ωm for tissue resistivity at FRC to 6.72 Ωm to 40 Ωm at total lung capacity (TLC).

In this work, we follow a different approach and derive a model for the electrical tissue resistivity directly based on the real alveolar microstructure of lung parenchyma. Using finite element simulations we are able to determine the effective resistivity by comparing the

electrical behaviour of resolved alveolar microstructures with the results of a homogenization approach.

2. Methods

To determine the resistivity of lung tissue, lungs from young adult rats are harvested according to Schittny *et al* (2008). After staining with heavy metals and paraffin embedding these samples are scanned in the TOMCAT beamline (SLS, Paul Scherrer Institut, Villigen, Switzerland) and a three-dimensional volume is reconstructed from the obtained images, enhancing the process described by Rausch *et al* (2011). The resulting alveolar walls are meshed with tetrahedral finite elements and stretched uniformly in all directions in a stepwise manner until the volume is increased by a factor of four. At each step of the simulation the air content of the cubical-shaped microstructure is calculated. Additionally, the current resulting from a potential difference between two opposite surfaces of the sample is measured. A correlation between resistivity of the tissue and alveolar air content is then derived following the procedure described in detail in the following sections.

2.1. Sample preparation, scanning and mesh generation

Sample preparation and scanning is performed following the protocol described in detail by Schittny *et al* (2008). The handling of animals before and during the experiments, as well as the experiments themselves, was approved by the local authorities. The process for segmentation of single alveolar wall structures from the scanned images described by Rausch *et al* (2011) is enhanced using the software package Amira 4.1.2 (Mercury Computer Systems). All enhancements are described in detail below.

Two regions of the scanned images are chosen as reference volumes of approximately the same size in order to account for the inhomogeneity in lung parenchyma due to the presence of small airways. The first sample is taken from a homogeneous tissue region (figure 1, left), whereas the second sample is extracted from a region that is crossed by a small airway at the top surface (figure 1, right). Segmentation is initially performed by using the 'magic wand' operations and corrected manually in locations where the automatic operations delivered poor quality. The surface of the resulting volume is triangulated and exported in STL file format. We might add that, as proven by Rausch *et al* (2011), the extracted volumes match morphological and morphometric data (Tschanz *et al* 2003).

To overcome the problem of sharp triangles resulting in poor numerical performance, a process to maximize mesh quality using the open source software MeshLab (Cignoni *et al* 2008) is established. First, the surface is subdivided with the 'Butterfly Subdivision' algorithm and cleaned from all remaining self-intersecting faces and holes if present. The result is a fine background mesh. Afterwards, a Poisson surface reconstruction (octree depth 11, solver divide 9) is applied to create a smooth and regular triangulated surface based on the geometry provided by the background mesh. One could now coarsen the surface mesh with the 'Quadric Edge Collapse Decimation' filter to reduce element size. In this simulations, however, the current mesh is used since the resulting element size has been proven to be spatially converged in previous studies (Rausch *et al* 2011). Finally the resulting surface triangulation is exported in STL format and 3D meshed in Gmsh (Geuzaine and Remacle 2009) using a Delaunay algorithm. The element size specified at the surface is kept for the volumetric meshing process. The six sides of the cubical-shaped sample were split into single surfaces to apply structural and electrical boundary conditions later. It is important to emphasize that, though the mesh

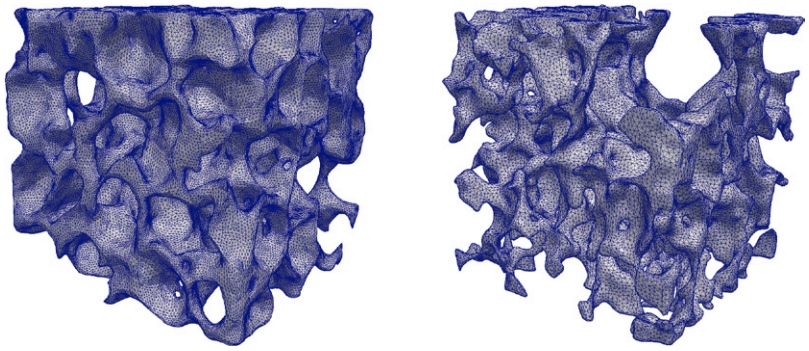

Figure 1. Reconstructed cubical-shaped volume meshes of synchrotron-based x-ray tomography scans of the alveolar microstructure. The left-hand sample is taken from a region of homogenous tissue, whereas the right-hand sample exhibits an inhomogeneity due to the crossing of a small airway at the top surface.

quality (see figure 2 for comparison) is improved significantly through our process, resulting in faster convergence and better performance of the simulations, the geometry of the alveolar wall ensembles has not changed. This is achieved by avoiding stronger smoothing operators such as Laplacian smoothing with high smoothing factors. Data on the final geometries are shown in table 1.

2.2. Structural simulation

Our simulations consist of two parts, namely a structural simulation which deforms the sample uniformly in all directions according to the governing equations of soft tissue mechanics, and an electrical simulation that applies a potential difference between two opposite surfaces of the stretched samples. Both algorithms are one-way coupled, meaning the structural deformation of the alveolar wall influences the potential distribution and the current flow throughout the tissue, whereas changes in potential and current obviously do not affect structural deformations. This reflects physical behaviour in reality.

The governing equations for soft tissue mechanics on the structural domain Ω^{S}, which is equal to the electrical domain Ω^{E}, are those of non-linear elastodynamics

$$\rho^{\mathrm{S}} \frac{d^2\mathbf{d}^{\mathrm{S}}}{\mathrm{d}t^2} = \nabla \cdot (\mathbf{F} \cdot \mathbf{S}) + \rho^{\mathrm{S}}\mathbf{b}^{\mathrm{S}} \text{ on } \Omega^{\mathrm{S}} \times [0, t] \tag{1}$$

where ρ^{S} denotes tissue density, $\mathbf{d}^{\mathrm{S}}$ the tissue displacements, $\mathbf{F} = \frac{\partial \mathbf{x}}{\partial \mathbf{X_0}}$ the deformation gradient, $\mathbf{S}$ the second Piola–Kirchhoff stresses and $\mathbf{b}^{\mathrm{S}}$ the body forces. Our material model uses a neo-Hookean-like strain energy function (Blatz and Ko 1962) based on the invariants of the right Cauchy–Green tensor $\mathbf{C} = \mathbf{F}^{\mathrm{T}}\,\mathbf{F}$, $I_1 = \mathrm{tr}(\mathbf{C})$ and $I_3 = \det(\mathbf{C})$

$$\Psi(\mathbf{C}) = \frac{E}{4-4\nu}(I_1 - 3) + \frac{E(1-2\nu)}{4\nu + 4\nu^2}\left(I_3^{-\frac{\nu}{1-2\nu}} - 1\right).$$

We use a Young's modulus of $E = 6.75$ kPa determined from previous experiments (Rausch *et al* 2011) and a Poisson's ratio of $\nu = 0.49$ to account for the incompressibility of the alveolar wall, mainly consisting of water. Tissue density ρ^{S} is therefore set to $\rho^{\mathrm{S}} = 1000$ kg m^{-3}. As mechanical boundary conditions we apply pure Dirichlet boundary conditions on all six surfaces of the cubical-shaped sample in order to deform the sample (edge length l) uniformly

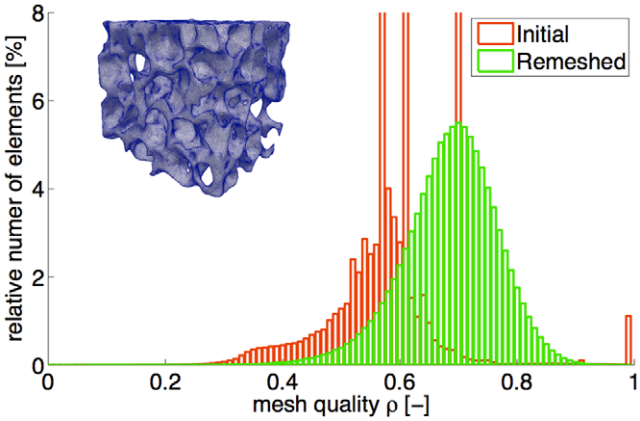

Figure 2. Mesh quality before (orange) and after the improved meshing strategy (green). The mesh quality ρ is defined as the ratio of the smallest edge to the largest edge of a tetrahedron. A mesh quality of $\rho = 1.0$ indicates an ideal tetrahedron.

Table 1. Properties of the mesh for the two alveolar wall geometries used in this study.

	Sample 1 'homogeneous'	Sample 2 'bronchiole'
Edge length l [μm]	200	210
Tissue volume V_{tissue} [μm^3]	2.7×10^6	2.0×10^6
Element size h [μm]	2.25	2.85
Number of elements	2 272 169	1 486 483
Degrees of freedom	1 428 708	940 599

in all dimensions (see figure 3). An equilibrium state is computed every $\Delta l = 10$ μm of prescribed boundary displacements up to the maximum stretch of $\Delta l = 100$ μm, which corresponds to a volume increase by a factor of almost four. At every step the air content and the tissue volume are computed in terms of the filling factor FF introduced by Nopp *et al* (1993)

$$\text{FF} = \frac{V_{\text{air}}}{V_{\text{tissue}}} = \frac{l^3 - V_{\text{tissue}}}{V_{\text{tissue}}} = \frac{l^3}{V_{\text{tissue}}} - 1 \tag{2}$$

and the deformed geometries serve as a basis for the electrical simulations as described in the next section.

2.3. Electrical simulation

For the electrical simulation the system is described by the Laplace equation

$$\nabla \cdot (-\sigma \nabla \Phi) = 0 \text{ on } \Omega^{\text{E}} \times [0, t] \tag{3}$$

giving a relation for the distribution of voltage $\Phi(\mathbf{x})$ in the domain Ω^{E} depending on the conductivity σ ($\mathbf{x}$). The potential is fixed on two opposite surfaces of the cubical-shaped sample (Dirichlet boundary conditions $\Gamma_{\text{D}}^{\text{E}}$). On the remaining surfaces, no-flux boundary conditions are applied. As a result of the applied potential difference a constant current flow on both surfaces ① and ② (see figure 4),

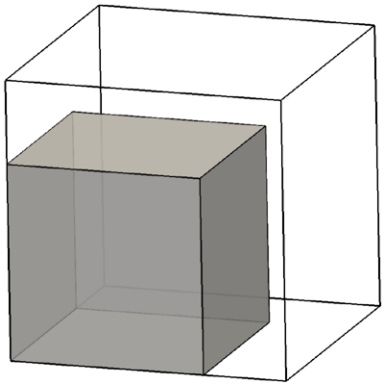

Figure 3. Illustration of uniform stretch in all three dimensions. The initial sample volume is shaded in grey while the current configuration at stretch is visualized in wireframe mode.

$$I = \int_{\Gamma^{\mathrm{D}}_{\mathrm{E},1/2}} (\sigma \nabla \Phi) \cdot \mathbf{n} \, \mathrm{d}A \tag{4}$$

can be measured in the simulations. For the conductivity $\sigma(\mathbf{x})$ the model introduced by Nopp *et al* (1993) and Nopp *et al* (1997) is used, where lung parenchyma consists of 85% blood-filled capillaries (conductivity $\sigma_{\mathrm{B}} = 0.655\ \Omega^{-1}\ \mathrm{m}^{-1}$), 12% epithelial cells (conductivity $\sigma_{\mathrm{E}} = 1.0\ \Omega^{-1}\ \mathrm{m}^{-1}$) and 3% intercellular fluid (conductivity $\sigma_{\mathrm{I}} = 2.0\ \Omega^{-1}\ \mathrm{m}^{-1}$). For the complete alveolar wall this results in a conductivity of $\sigma_{\mathrm{Alv}} = 0.7284\ \Omega^{-1}\ \mathrm{m}^{-1}$. The applied potential difference is $U = \Phi_1 - \Phi_2 = 10$ V and one quasi-static electrical step is required until the simulation is converged.

All simulations are performed in our in-house multiphysics code *BACI* (Wall and Gee 2014) and the electrical problem is solved in every 10 μm increment of the structural problem. The deformed alveolar geometry is automatically updated before each electrical simulation.

2.4. Correlation between resistivity and filling factor

The electrical simulations of different deformation states can be used to find a link between the local resistivity of the lung tissue sample and its air content. For this purpose a homogenization approach (see, e.g. Bear and Bachmat (1990) and Vuong *et al* (2014)) is used to replace the resolved porous microgeometry by a uniform domain as depicted in figure 4 (right). By this approach, the influence of the porous structure on the current flow is modelled by the so-called effective conductivity σ_{eff}, which depends on two additional geometrical parameters contributing to the alveolar wall conductivity σ_{Alv} (see, e.g. Holzer *et al* (2013))

$$\sigma_{\mathrm{eff}} = \frac{\varepsilon}{\tau(\varepsilon)} \sigma_{\mathrm{Alv}} \tag{5}$$

where ε denotes the volume fraction of the alveolar wall and $\tau(\varepsilon)$ the tortuosity depending on the actual state of sample deformation. As explained, e.g. by Clennell (1997), the tortuosity can be seen as an elongation of the current paths as a result of the porous microstructure in relation to the shortest straight line distance l between surfaces ① and ②. In this specific case, τ is called the geometrical tortuosity. The volume fraction ε of the alveolar wall is defined as

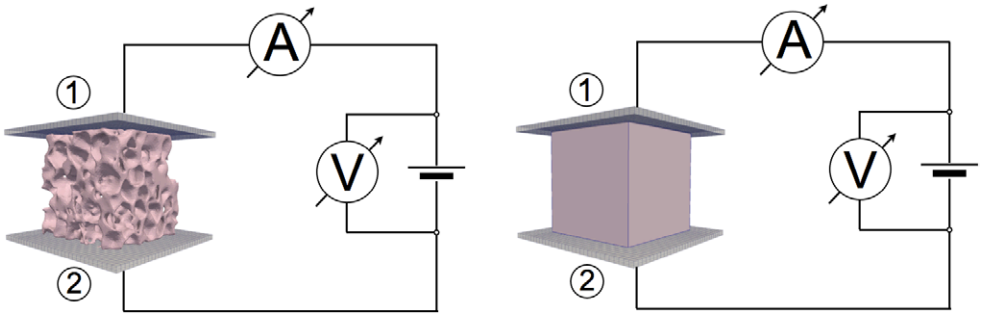

Figure 4. Electrical simulation setup. A known potential difference is applied between opposite surfaces of the cubical-shaped alveolar microstructure (left) and the homogenized sample (right). The corresponding current flow between surfaces 1 and 2 is measured.

$$\varepsilon = \frac{V_{\text{tissue}}}{V_{\text{air}} + V_{\text{tissue}}} = \frac{V_{\text{tissue}}}{l^3}$$

and can be reformulated in terms of the filling factor FF

$$\varepsilon = (\text{FF} + 1)^{-1}.$$

Consequently, equation (5) can be also written as a relation between the local effective resistivity $\rho_{\text{eff}} = \frac{1}{\sigma_{\text{eff}}}$ and the local filling factor

$$\rho_{\text{eff}} = \frac{\tau(\varepsilon)}{\sigma_{\text{Alv}}}(\text{FF} + 1) \tag{6}$$

depending only on the alveolar wall conductivity and the tortuosity. In order to use equation (6) as a quantitative link between resistivity and filling factor, it is necessary to determine the tortuosity for a representative sample of lung tissue. If the representativeness of the samples is guaranteed, the homogenization approach as well as the correlation in equation (6) is also applicable to the entire lung volume.

From the known potential difference $U = \Phi_1 - \Phi_2$ and the measured current flow $I(\varepsilon)$ the actual resistance of the tissue volume can be calculated based on Ohm's law

$$R = \frac{U}{I(\varepsilon)}. \tag{7}$$

As shown, e.g. by Wiedenmann *et al* (2013), the resistance can also be expressed in terms of the effective conductivity

$$R = \frac{1}{\sigma_{\text{eff}}}\frac{l}{A} = \frac{1}{\sigma_{\text{Alv}}}\frac{\tau(\varepsilon)}{\varepsilon}\frac{l}{A} \tag{8}$$

where l is the edge length and A the cross-sectional area of the sample. By comparison of equation (7) and equation (8) the tortuosity of the homogenized sample can be calculated as

$$\tau(\varepsilon) = \varepsilon\sigma_{\text{Alv}}\frac{A}{l}\frac{U}{I(\varepsilon)}. \tag{9}$$

It is important to emphasize that all microstructural effects influencing the conductivity, e.g. the variation of pore diameter or the roughness of the wall, are incorporated into the tortuosity

Table 2. Geometrical and electrical parameters in the undeformed state for both geometries.

	Sample 1 'homogeneous'	Sample 2 'bronchiole'
Volume fraction of tissue ε	0.319	0.214
Filling factor FF	2.10	3.66
Current flow I^X [mA]	0.269 44	0.1367
Current flow I^Y [mA]	0.272 56	0.147 86
Current flow I^Z [mA]	0.266 24	0.1474
Mean tortuosity $\bar{\tau}$	1.71	2.27

calculated from equation (9) (see, e.g. Wiedenmann *et al* (2013)). As a result, the tortuosity τ cannot be interpreted anymore as a pure elongation of the current path. To underline this, the tortuosity calculated from equation (9) is called the electrical tortuosity. However, equation (9) is still valid and can be applied to the entire lung tissue as long as the sample with all microstructural effects is representative.

3. Results

3.1. Undeformed state

In table 2 the tissue volume fraction ε, the filling factor FF and the direction-dependent current flow I throughout the cubical-shaped alveolar geometries in all three directions (i.e. X, left–right; Y, bottom–top, Z, front–back) in the initial undeformed state are listed. Based on these values equation (9) is used to calculate the direction-dependent tortuosity to investigate any anisotropic effects of the microstructure. While the homogeneous sample shows almost no dependence on the direction of applied voltage ($\tau^X = 1.715$, $\tau^Y = 1.711$, $\tau^Z = 1.720$), the geometry crossed by the small airway shows higher absolute values and slight variations in the tortuosity ($\tau^X = 2.39$, $\tau^Y = 2.21$, $\tau^Z = 2.20$). The mean tortuosities $\bar{\tau}$ for both samples averaged over all three directions are listed in table 2.

3.2. Linear model during stretch

Assuming that the mean tortuosity $\bar{\tau}$ remains constant during stretching of the sample (an assumption that we will investigate below), equation (6) is reduced to the following linear relation (equation (10)) and can be used to calculate the mean effective resistivity $\bar{\rho}_{\text{eff}}$ for both samples in the range of FF $\in$ [1.0; 8.0].

$$\bar{\rho}_{\text{eff}} = \frac{\bar{\tau}}{\sigma_{\text{Alv}}} (\text{FF} + 1). \tag{10}$$

Physiological filling factors are usually in the range of 2.0–6.0 (Nopp *et al* 1993). The resulting resistivities for both samples are plotted in figure 5 in comparison with previous studies, and will be discussed in detail in the subsequent section.

3.3. Nonlinearity of the tortuosity

In general, the tortuosity $\tau(\varepsilon)$ is dependent on the volume fraction ε. To verify the above assumption of a constant tortuosity during stretch, the effective resistivity ρ_{eff} is determined

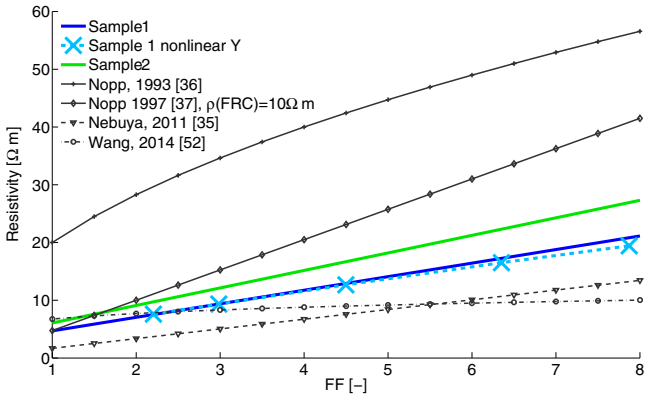

Figure 5. Results for the resistivity dependence on the filling factor in our model and in literature.

by equation (6) based on the deformation-dependent tortuosity $\tau(\varepsilon)$, which is calculated from equation (9) after each increment in the structural simulation. The result is shown exemplarily for the *Y*-direction of sample 1 in figure 5 (denoted as sample 1 nonlinear Y). It can be seen that the values for the specific resistivity lie almost on the line for the linear model and that they only start to differ slightly at very high filling factors corresponding to high values of stretch. This congruity supports the validity of the above assumption that a linear model during stretch is suitable and will be discussed in detail in section 4. In figure 6 the deformations of the homogeneous alveolar geometry at five different steps of the simulation, corresponding to the cross markers on the magenta line in figure 5, are shown. Elongation and thinning of the single alveolar walls, which are the main reasons for changes in tissue resistivity, can be seen with increasing air content in the sample. Tissue volume V_{tissue} itself does not change due to incompressibility.

3.4. Application to EIT data measured at the bedside

Figure 7 compares the measured EIT derived (left) and the computed (right) changes of tissue resistivity ρ_{eff} in one mechanically ventilated patient monitored by EIT at the bedside. They represent total lung capacity (TLC) referenced to EELV at the set PEEP level. Patient EIT data (left) were acquired using the PulmoVista® 500 device (Dräger medical, Lübeck, Germany). The electrode belt (containing 16 electrodes) was attached around the patient's chest circumference at the level of the fifth intercostal space. The EIT data were acquired at a scan rate of 50 images/s. The patient was on pressure-controlled ventilation with a positive end-expiratory pressure of 7 cm H_2O and a tidal volume of 6 ml kg^{-1} predicted body weight. The right image shows the image at the same position computed with our resistivity model coupled to a well validated reduced-dimensional human lung model (Ismail *et al* 2013). For better comparison, both images are shown with the same colour coding. Using this reduced-dimensional lung model, local acinar volumes are computed based on patient-specific CT data acquired 24 h prior to the EIT examination and the applied ventilation profile. For more details on this method see Ismail *et al* (2013). The resistivity distribution is calculated from the local filling factor FF, based on local acinar volumes, and the constant tortuosity of the homogeneous sample with the previously derived parameters $\bar{\tau} = 1.71$, $\sigma_{\text{Alv}} = 0.7284\ \Omega^{-1}\ \text{m}^{-1}$. The resistivity ρ_{eff} ranges from −4 to 8 in both images and shows good agreement in the local patterns of

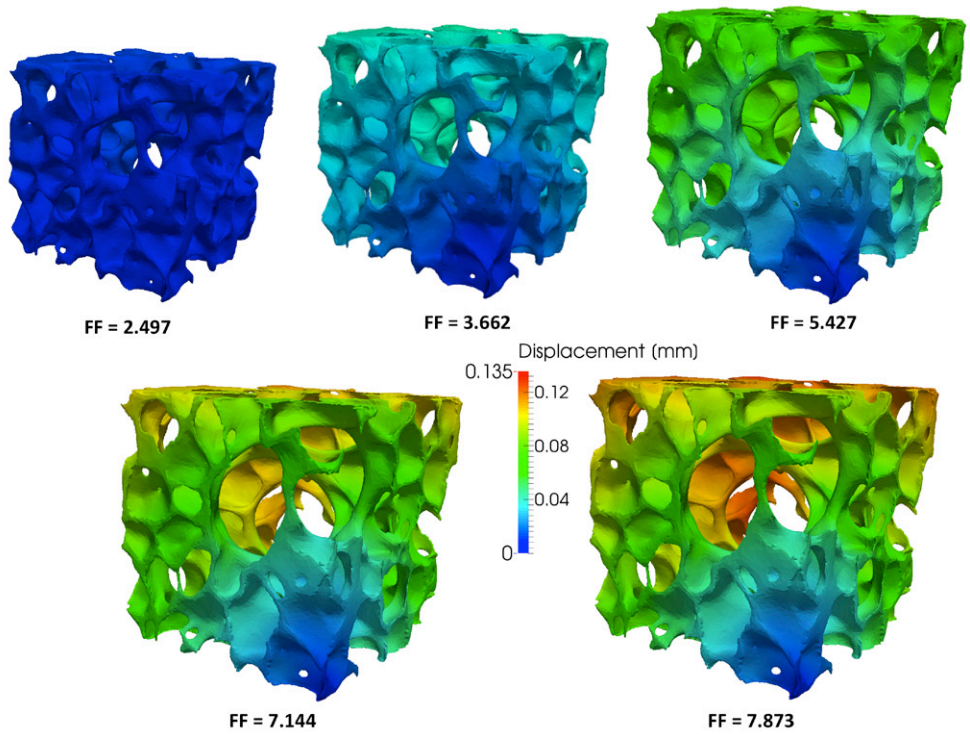

Figure 6. Displacement of the homogeneous alveolar microstructure in five states. Elongation and thinning of the alveolar wall structures during stretch can be observed.

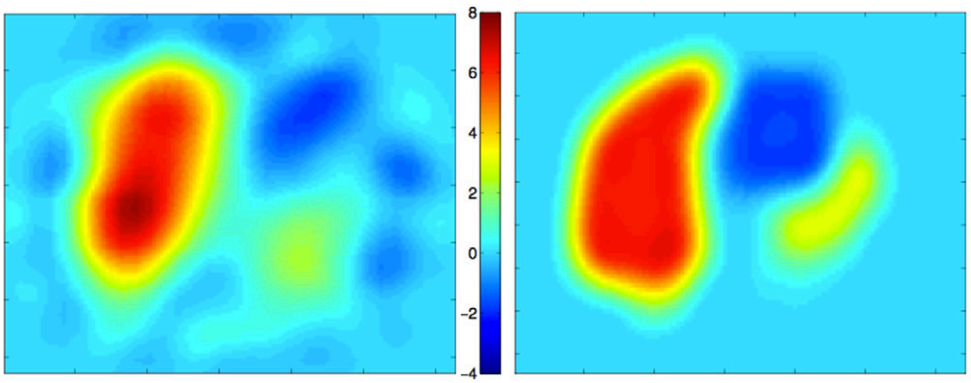

Figure 7. Comparison of local tissue resistivity determined from EIT measurements at the bedside (left) and computed resistivity values for known filling factors (right). Red pixel values indicate positive resistivity changes against the baseline state due to inspiration, yellow indicates regions of lower ventilation and dark blue values show the resistivity changes attributable to cardiac activity.

ventilation, even though they do not match exactly. This can be explained by the neglect of surrounding soft tissues, which clearly has an influence on the image reconstruction (Adler and Lionheart 2006).

4. Discussion

The main finding of this study is that a linear relationship for effective tissue resistivity ρ_{eff} based on the filling factor FF is justified in a clinical setting. This correlation, which was also observed phenomenologically on a macroscopic scale, is now reconfirmed, exploiting the physics of the parenchyma microstructure in a finite element simulation. All parameters in the relationship are physically based and either can be measured directly or are inherent in the geometry. Further enhancements to previously existing approaches have been made in this work, e.g. an upper and lower bound for tissue resistivity, and will be discussed in detail in the following.

4.1. Correction of the filling factor

Nopp *et al* (1993) determined filling factors from two-dimensional microscopy images, stating that values of FF = 2.0 correspond to FRC and FF = 4.0 to TLC. However, they already present samples with higher air content at FRC (FF > 3) in their publication. Following the observations from our 3D geometries, filling factors of FF = 2.0 for FRC and FF = 4.0 for TLC seem to be quite low compared to our geometries, showing values of FF = 2.1 for the homogeneous and FF = 3.66 for the heterogeneous microstructure in the unstretched state. Considering the fact that a three-dimensional determination is probably more exact as it averages tissue structure over a larger representative volume than a two-dimensional image slice, we rather propose a filling factor of FF = 3.0 at FRC and FF = 6.0 at TLC determined from our stretched geometries. This is in line with parenchyma density calculations based on a lung tissue density of $\rho_{\text{t}} = 1050\ \text{kg m}^{-3}$ (Boyd 1962) and a homogenized density of $\rho^{\text{S}}_{\text{FRC}} = 246\ \text{kg m}^{-3}$ (de la Grandmaison *et al* 2001, Nebuya *et al* 2011), which results in a filling factor of

$$\text{FF}_{\text{FRC}} = \frac{\rho_{\text{t}}}{\rho^{\text{S}}_{\text{FRC}}} - 1 = 3.26.$$

This also holds for the observed homogenized lung density $\rho^{\text{S}}_{\text{TLC}} = 142.1\,\text{kg m}^{-3}$ at TLC and results in a filling factor of $\text{FF}_{\text{TLC}} = 6.38$ (Nebuya *et al* 2011), supporting the range of filling factors we observed over a relatively large anatomical spectrum.

4.2. Isotropy of the electrical macroscale behaviour

Within our two alveolar microstructures we investigated possible dependences on the direction of the applied voltage by measuring the current flow in all three directions throughout the samples. In the homogeneous geometry, we did not observe any anisotropy of electrical properties of the tissue, meaning that the irregular arrangement of alveoli shows an isotropic electrical behaviour on the macroscale. This result indicates that the sample can be considered as representative. Even in case of a clearly visible inhomogeneity such as a small airway, reducing the tissue volume locally by around one-third compared to the homogeneous structure, we observe only small deviations of the current flow dependent on the direction and on the corresponding tortuosity. Furthermore, small airways such as the one that crosses the heterogeneous sample are not located at tissue boundaries, but embedded in lung parenchyma in order to supply the surrounding alveoli with air. This surrounding tissue will further damp the influence of the inhomogeneity investigated in this study. Finally, neither microgeometry shows a respectable anisotropy in any direction of preferred current

in the sample. This justifies an isotropic homogenized model for the effective resistivity of lung tissue *in vivo*.

4.3. Nonlinear versus linear relation

In general, the tortuosity $\tau(\varepsilon)$ is a function of the tissue volume fraction, since any deformation of the sample leads to a change in the characteristics of the microstructure. However, the results of the finite element simulations show that the approximation by a linear law is justified within the physiological range of stretch, which implies that the tortuosity remains almost constant in this range. The reason is that the uniform deformation in all spatial directions does not change the ratio between the current path length and the edge length of the deformed sample significantly. Only at relatively high stretches beyond the physiological range (FF $>$ 6.0) do the alveolar walls start aligning in the direction of the current, which shortens the path of the current relative to the edge length of the deformed sample. This effect has already been experimentally observed by Nopp *et al* and modelled by a root function for the relation between tissue resistivity and filling factor (Nopp *et al* 1993).

4.4. Comparison with literature and bedside data

The linear relationship between filling factor FF and tissue resistivity ρ_{eff} described in our study shows good agreement with previously published models (Nopp *et al* 1993, Nopp *et al* 1997, Nebuya *et al* 2011, Wang *et al* 2014), as shown in figure 5. All presented models except for the first one by Nopp *et al* (1993) exhibit almost the same initial resistivity value at FF = 1.0. However, Nopp *et al* (1993) mention local hyperinflation as one possible limitation in their experiments leading to higher overall values of resistivity at a reasonable slope. The idea of local hyperinflation is supported by the noticeable nonlinearity in their measurements, which is also observed in our geometry at high filling factors corresponding to hyperinflation. The second model by Nopp *et al* (1997) is based on a model of single cubical-shaped alveoli representing the electrical conductivity of the alveolar walls. While the initial value shows good agreement, the gradient of the curve is higher than those observed in other studies. This might be due to the simplification of single alveoli as thin-walled cubes. As already proposed by Mead *et al* (1970) and apparent in our scanned geometries, the alveolar ensembles are rather irregular and might be better approximated using tetrakaidecahedra. Nebuya *et al* (2011) adopt the thin-walled cube alveolus model of Nopp *et al* (1997) and vary the conductivity of the walls, obtaining a lower slope and a slightly lower initial value than presented in the original study. In the work by Wang *et al* (2014), the resistivity remains almost constant throughout the complete range of filling factors. Assuming that this curve would show fairly small variation of tissue resistivity dependent on the filling factor, it would become rather difficult to reconstruct EIT images during respiration (Adler and Lionheart 2006). Finally, our model provides a reasonable range for the effective resistivity in different lung aeration states compliant with previously published data tightening the widely varying values in literature. The upper and lower bounds provided by our model correspond to a homogeneous microstructure in the respiratory zone and to an inhomogeneous microstructure with embedded airways that can be found in the conducting zone of the respiratory system. When applied to real patient data the linear relationship for the homogeneous sample can reproduce clinical resistivity measurements obtained from EIT. This supports the fact that our correlation can be applied to gain further insight into local ventilation patterns in a clinical setting.

4.5. Impact of the study and further work

One major perspective of the method described in this study lies in EIT examination of pathophysiological states, e.g. if the lung of a patient is filled with water as in lung oedema. In these cases, it is not assured that the current solely flows through the alveolar cells but it can also be conducted by the liquid medium. While other methods might not be fully able to capture this effect, it can easily be included in our approach. One can simply 'fill' the air spaces, which are currently assumed to contain insulating air, with a liquid medium such as extracellular fluid, blood or mucus and assign the corresponding conductivities as described in section 2. The calculated current will then directly take the combination of alveolar wall, air content and liquid medium into account. This can be used to investigate tissue resistivity in cases of pulmonary oedema, infarction or mucus accumulation in the future. Similar research potential lies in a scenario when alveoli collapse as in lung atelectasis and, consequently, the characteristic of the microstructure changes. In these cases the linear link between alveolar ventilation and regional tissue resistivity might no longer be valid due to emerging shunts. Further investigations are required to study these phenomena. However, these pathophysiological scenarios are extremely interesting in a clinical setting as they severely damage the parenchyma (Tobin 2001). They offer undeveloped potential for the extension of the method described in this publication. This study provides a tool for direct bedside calculation of local alveolar ventilation from EIT measurements. This method gives physicians immediate information on a patient's local air distribution in response to different ventilatory patterns, enabling a better, direct assessment of the patient–ventilator interaction.

5. Conclusion

In this article finite element simulations on lung parenchyma microgeometries are used to prove that a linear approximation between alveolar air content and effective tissue resistivity ρ_{eff} is justified as a quantitative link between lung tissue bioimpedance and the amplitude of alveolar ventilation. All parameters included in the relationship are physically based. The conductivity of the alveolar wall σ_{Alv} can be measured experimentally and the mean tortuosity $\bar{\tau}$ is a pure geometrical property of the alveolar microstructure. Based on simulations of real alveolar wall geometries, an upper and a lower bound for tissue resistivities spanning various states of lung aeration are determined in this study. While the values reported in the literature exhibit high variability, the presented method grounded on true lung anatomy can be expected to render more precise data. Finally, the linear approximation is applied to a realistic simulation within a clinical setting and matches EIT data measured at the bedside. We conclude that this work presents a direct link between EIT-measured tissue impedance and the command variable for mechanical ventilation, i.e. regional air content. With this knowledge ventilation parameters can be adjusted more carefully, resulting in more protective protocols, especially in pathophysiology where the insight provided by other methods is limited.

Acknowledgments

We gratefully acknowledge the computational resources provided by the Leibniz Supercomputing Center under project pr32ne 'Coupled problems in computational modeling of the respiratory system'. Furthermore, the help of Marco Stampanoni, Swiss Light Source, Paul Scherrer Institute, Villigen, Switzerland, in obtaining the scanned sample geometries is gratefully acknowledged.

References

Adler A *et al* 2009 GREIT: a unified approach to 2D linear EIT reconstruction of lung images, *Physiol. Meas.* **30** 35–55

Adler A and Lionheart W R B 2006 Uses and abuses of EIDORS: an extensible software base for EIT *Physiol. Meas.* **27** 25–42

Adler A *et al* 2012 Whither lung EIT: Where are we, Where do we want to go and What do we need to get there? *Physiol. Meas.* **33** 679–94

Barber D C 1989 A review of image reconstruction techniques for electrical impedance tomography *Med. Phys.* **16** 162–9

Bayford R, Kantartzis P, Tizzard A, Yerworth R, Liatsis P and Demosthenous A 2008 Development of a neonate lung reconstruction algorithm using a wavelet AMG and estimated boundary form *Physiol. Meas.* **29** S125

Bear J and Bachmat Y 1990 *Introduction to Modeling of Transport Phenomena in Porous Media* (Berlin: Springer)

Blaser D, Pulletz S, Becher T, Schadler D, Elke G, Weiler N and Frerichs I 2014 Unilateral emphysema impacts the assessment of regional lung ventilation by electrical impedance tomography *Physiol. Meas.* **35** 975–83

Blatz P J and Ko W L 1962 Application of finite elastic theory to the deformation of rubbery materials *Trans. Soc. Rheol.* **6** 223–51

Bodenstein M, David M and Markstaller K 2009 Principles of electrical impedance tomography and its clinical application *Crit. Care Med.* **37** 713–24

Boyd E 1962 *Growth, Including Reproduction and Morphological Development Biological Handbooks* Altmann P and Dittmer D S (Washington, DC: Federation of American Societies for Experimental Biology) pp 346–8

Brown B H, Barber D C, Morice A H and Leathard A D 1994 Cardiac and respiratory related electrical impedance changes in the human thorax *IEEE Trans. Biomed. Eng.* **41** 729–34

Brown B H 2003 Electrical impedance tomography (EIT): a review *J. Med. Eng. Technol.* **27** 97–108

Cignoni P, Corsini M and Ranzuglia G 2008 MeshLab: an Open-Source 3D Mesh Processing System *ERCIM News* **73** 45–6

Clennell M B 1997 Tortuosity: a guide through the maze *Geol. Soc.* **122** 299–344 (special publications)

Erlandsson K, Odenstedt H, Lundin S and Stenqvist O 2006 Positive end-expiratory pressure optimization using electric impedance tomography in morbidly obese patients during laparoscopic gastric bypass surgery *Acta Anaesthesiol. Scand.* **50** 833–9

Frerichs I 2000 Electrical impedance tomography (EIT) in applications related to lung and ventilation: a review of experimental and clinical activities *Physiol. Meas.* **21** R1–21

Frerichs I, Becher T and Weiler N 2014 Electrical impedance tomography imaging of the cardiopulmonary system *Curr. Opin. Crit. Care* **20** 323–32

Gabriel C, Gabriel S and Corthout E 1996a The dielectric properties of biological tissues: I. Literature survey *Med. Phys. Biol.* **41** 2231–49

Gabriel S, Lau R and Gabriel C 1996b The dielectric properties of biological tissues: II. Measurements in the frequency range 10 Hz to 20 GHz *Med. Phys. Biol.* **41** 2251–69

Geuzaine C and Remacle J-F 2009 Gmsh: a three-dimensional finite element mesh generator with built-in pre- and post-processing facilities *Int. J. Numer. Eng.* **79** 1309–31

de la Grandmaison, G L , Clairand I and Durigon M 2001 Organ weight in 684 adult autopsies: new tables for a Caucasoid population *Forensic Sci. Int.* **119** 149–54

Gomez-Laberge C, Rettig J S, Smallwood C D, Boyd T K, Arnold J H and Wolf G K 2013 Interaction of dependent and non-dependent regions of the acutely injured lung during a stepwise recruitment manoeuvre *Physiol. Meas.* **34** 163

Hahn G, Just A, Hellige G, Dittmar J and Quintel M 2013 How absolute EIT reflects the dependence of unilateral lung aeration on hyper-gravity and weightlessness? *Physiol. Meas.* **34** 1063

Hinz J, Neumann P, Dudykevych T, Andersson L G, Wrigge H, Burchardi H and Hedenstierna G 2003 Regional ventilation by electrical impedance tomography: a comparison with ventilation scintigraphy in pigs *Chest* **124** 314–22

Holzer L, Wiedenmann D, Münch B, Keller L, Prestat M, Gasser Ph, Robertson I and Grobéty B 2013 The influence of constrictivity on the effective transport properties of porous layers in electrolysis and fuel cells *J. Mater. Sci.* **48** 2934–52

Ismail M, Comerford A and Wall W A 2013 Coupled and reduced dimensional modeling of respiratory mechanics during spontaneous breathing *Int. J. Numer. Methods Biomed. Eng.* **29** 1285–305

Luepschen H, Meier T, Grossherr M, Leibecke T, Karsten J and Leonhardt S 2007 Protective ventilation using electrical impedance tomography *Physiol. Meas.* **28** 247–60

Lupton-Smith A R, Argent A C, Rimensberger P C and Morrow B M 2014 Challenging a paradigm: positional changes in ventilation distribution are highly variable in healthy infants and children *Pediatr. Pulmonol.* **49** 764–71

Mauri T, Bellani G, Confalonieri A, Tagliabue P, Turella M, Coppadoro A, Citerio G, Patroniti N and Pesenti A 2013 Topographic distribution of tidal ventilation in acute respiratory distress syndrome: effects of positive end-expiratory pressure and pressure support *Crit. Care Med.* **41** 1664–73

Mead J, Takishima T and Leith D 1970 Stress distribution in lungs: a model of pulmonary elasticity *J. Appl. Physiol.* **28** 596–608

Miedema M, de Jongh F H, Frerichs I, van Veenendaa M B and van Kaam A H 2012 The effect of airway pressure and oscillation amplitude on ventilation in pre-term infants *Eur. Respir. J.* **40** 479–84

Muders T *et al* 2012 Tidal recruitment assessed by electrical impedance tomography and computed tomography on a porcine model of lung injury *Crit. Care Med.* **40** 903–11

Nebuya S, Mills G H, Milnes P and Brown B H 2011 Indirect measurement of lung density and air volume from electrical impedance tomography (EIT) data *Physiol. Meas.* **32** 1953–67

Nopp P, Harris N D and Brown B H 1997 Model for the dielectric properties of human lung tissue against frequency and air content *Med. Biol. Eng. Comput.* **35** 695–702

Nopp P, Rapp E, Pfützner H, Nakesch H and Ruhsam Ch 1993 Dielectric properties of lung tissue as a function of air content *Phys. Med. Biol.* **38** 699–716

Nguyen D T, Jin C, Thiagalingam A and McEwan A L 2012 A review on electrical impedance tomography for pulmonary perfusion imaging *Physiol. Meas.* **33** 695–706

Rausch S M K, Haberthür D, Schittny J C and Wall W A 2011 Local strain distribution in real three-dimensional alveolar geometries *Ann. Biomed. Eng.* **39** 2835–43

Rausch S M K, Martin C, Bornemann P B, Uhlig S and Wall W A 2011 Material model of lung parenchyma based on precision-cut lung slice testing *J. Mech. Behav. Biomed.* **4** 583–92

Reifferscheid F, Elke G, Pulletz S, Gawelczyk B, Lautenschlager I, Steinfath M, Weiler N and Frerichs I 2011 Regional ventilation distribution determined by electrical impedance tomography: reproducibility and effects of posture and chest plane *Respirology* **16** 523–31

Riedel T, Kyburz M, Latzin P, Thamrin C and Frey U 2009 Regional and overall ventilation inhomogeneities in preterm and term-born infants *J. Intensive Care Med.* **35** 144–51

Rush S, Abildskov J A and McFee R 1963 Resistivity of body tissues at low frequencies *Circulation* **22** 40–50

Schittny J C, Mund S I and Stampanoni M 2008 Evidence and structural mechanism for late lung alveolarization *Am. J. Physiol. Lung Cell Mol. Physiol.* **294** 246–54

Schwan H P and Kay C F 1956 Specific resistance of body tissues *Circ. Res.* **4** 664–70

Tobin M D 2001 Advances in mechanical ventilation *New Engl. J. Med.* **344** 1986–96

Tschanz S A, Makanya A N, Haenni B and Burri P H 2003 Effects of neonatal high-dose short-term glucocorticoid treatment on the lung: a morphologic and morphometric study in the rat *Pediatr. Res.* **53** 72–80

Victorino J A *et al* 2004 Imbalances in regional lung ventilation: a validation study on electrical impedance tomography *Am. J. Respir. Crit. Care Med.* **169** 791–800

Vogt B, Pulletz S, Elke G, Zhao Z, Zabel P, Weiler N and Frerichs I 2012 Spatial and temporal heterogeneity of regional lung ventilation determined by electrical impedance tomography during pulmonary function testing *J. Appl. Physiol.* **113** 1154–61

Vuong A-T, Yoshihara L and Wall W A 2014 A general approach for modeling interacting flow through porous media under finite deformations *Comput. Methods Appl. Mech. Eng.* **283** 1240–59

Wall W A and Gee M 2014 Baci: a parallel multiphysics simulation environment *Technical Report* Institute for Computational Mechanics, TUM

Wang J-R, Sun B-Y, Wang H-X, Pang S, Xu X and Sun Q 2014 Experimental study of dielectric properties on human lung tissue *in vitro J. Med. Biol. Eng.* **34** 598–604

Wiedenmann D *et al* 2013 Three-dimensional pore structure and ion conductivity of porous ceramic diaphragms *AIChE J.* **59** 1446–57

Wolf G K, Gomez-Laberge C, Rettig J S, Vargas S O, Smallwood C D, Prabhu S P, Vitali S H, Zurakowski D and Arnold J H 2013 Mechanical ventilation guided by electrical impedance tomography in experimental acute lung injury *Crit. Care Med.* **41** 1296–304

Wrigge H, Zinserling J, Muders T, Varelmann D, Günther U, von der Groeben C, Magnusson A, Hedenstierna G and Putensen C 2008 Electrical impedance tomography compared with thoracic computed tomography during a slow inflation maneuver in experimental models of lung injury *Crit. Care Med.* **36** 903–9

Yoshida T, Torsani V, Gomes S, De Santis R R, Beraldo M A, Costa E L V, Tucci M R, Zin W A, Kavanagh B P and Amato M B P 2013 Spontaneous effort causes occult pendelluft during mechanical ventilation *Am. J. Respir. Crit. Care Med.* **188** 1420–7

Zhang J and Patterson R 2010 Non-invasive determination of absolute lung resistivity in adults using electrical impedance tomography *Physiol. Meas.* **31** 45–56